

# Space-local memory in generalized master equations: Reaching the thermodynamic limit for the cost of a small lattice simulation

Srijan Bhattacharyya,<sup>1</sup> Thomas Sayer,<sup>1,2</sup> and Andrés Montoya-Castillo<sup>1, a)</sup>

<sup>1)</sup>*Department of Chemistry, University of Colorado Boulder, Boulder, CO 80309, USA*

<sup>2)</sup>*Department of Chemistry, Durham University, Durham DH1 3LE, United Kingdom*

(Dated: 14 November 2024)

The exact quantum dynamics of lattice models can be computationally intensive, especially when aiming for large system sizes and extended simulation times necessary to converge transport coefficients. By leveraging finite memory times to access long-time dynamics using only short-time data, generalized master equations (GMEs) can offer a route to simulating the dynamics of lattice problems efficiently. However, such simulations are limited to small lattices whose dynamics exhibit finite-size artifacts that contaminate transport coefficient predictions. To address this problem, we introduce a novel approach that exploits finite memory in time *and* space to efficiently predict the many-body dynamics of dissipative lattice problems involving short-range interactions. This advance enables one to leverage the short-time dynamics of small lattices simulate arbitrarily large systems over long times. We demonstrate the strengths of this method by focusing on nonequilibrium polaron relaxation and transport in the dispersive Holstein model, successfully simulating lattice dynamics in one and two dimensions free from finite-size effects, reducing the computational expense of such simulations by multiple orders of magnitude. Our method is broadly applicable and provides an accurate and efficient means to investigate nonequilibrium relaxation with microscopic resolution over mesoscopic length and time scales that are relevant to experiment.

## I. INTRODUCTION

Lattice models play a key role in understanding physical and chemical phenomena. For instance, the Holstein<sup>1,2</sup> and Fröhlich<sup>3</sup> models shed light on polaron formation and electrical transport in semiconductors,<sup>4,5</sup> the Hubbard model<sup>6</sup> helps elucidate the mechanisms of high-temperature superconductivity,<sup>7</sup> and the Ising model<sup>8</sup> is used to interrogate magnetism<sup>9</sup> and phase transitions.<sup>10</sup> However, while modern algorithms can efficiently simulate the quantum dynamics of small lattices over short times,<sup>11–27</sup> reaching sufficiently large systems and long times to compare to experiments remains a fundamental challenge. This is because these methods often scale exponentially or, at best, polynomially with lattice size and simulation time, rendering the thermodynamic limit inaccessible.

The severity of this limitation becomes clear when calculating dynamic properties, e.g., conductivities, viscosities, and diffusion constants, which are sensitive to finite-size effects.<sup>28–35</sup> For example, finite-size effects can cause simulations to underestimate diffusion constants of polymers near the glass-transition,<sup>36</sup> relaxation times of glass-forming liquids,<sup>37</sup> the Curie temperature for Ni nanoparticles,<sup>38</sup> and the diffusion constant and viscosity of model fluids,<sup>39</sup> overestimate the critical fermion-phonon coupling causing the metal-to-Peierls phase transition in a Holstein-Hubbard lattice;<sup>40</sup> and yield apparently non-converging mobilities of dispersive Holstein polarons.<sup>41</sup> These examples reveal the need of computing the dynam-

ics of lattice models in thermodynamically large systems over long timescales.

Generalized Master Equations (GMEs) have emerged as a powerful tool for reducing the computational cost of dynamical simulations.<sup>42–61</sup> GMEs are exact non-Markovian equations of motion for nonequilibrium averages, correlation functions, and even multi-time correlators of select variables that encapsulate the effects of an environment into a memory kernel.<sup>62–64</sup> In dissipative systems, the memory kernel decays to zero over a finite memory lifetime, which can be shorter than the relaxation time of the desired correlation function. Thus, in principle, one can use a reference simulation over the memory lifetime to construct a GME that predicts the dynamics of the desired correlation function to arbitrarily long times. This temporal truncation of memory at its lifetime can reduce the computational cost of simulating the quantum or classical dynamics of complex many-body systems in different problems, including charge transfer reactions in solution,<sup>65,66</sup> protein folding,<sup>67–69</sup> nonlinear spectroscopy,<sup>60,70</sup> and transport.<sup>71,72</sup> However, to construct a GME from a short-time reference simulation, it must satisfy two conditions: (1) the simulation time must span the memory kernel lifetime, and (2) the reference calculation must be performed in the same system whose dynamics one intends to interrogate with the GME. If one constructs a GME using a small lattice simulation, particles encounter the lattice boundaries and manifest finite-size effects: one reduces the cost but still obtains the wrong answer. Hence, one must be able to afford an admittedly short-time reference simulation, but of a thermodynamically large lattice. The poor scaling of dynamical methods with system size renders this calculation at best impractical and at worst impossible.

a) [Andres.MontoyaCastillo@colorado.edu](mailto:Andres.MontoyaCastillo@colorado.edu)

Here, we propose a novel approach to lattice problems that exploits our observation that certain GME formulations display a *finite spatial memory* to motivate truncating memory in time *and* space. This allows us to employ short-time reference simulations of small lattices to generate the exact quantum dynamics of thermodynamically large lattices over arbitrarily long times for the cost of only the small reference calculation. We demonstrate the strengths of this method by applying it to nonequilibrium polaron formation and transport in dispersive Holstein lattices. Enabled by our space-local GME, we simulate, for the first time, the exact nonequilibrium quantum dynamics of small polaron formation, relaxation, and flow in thermodynamically large one-(1D) and two-dimensional (2D) lattices with up to 900 sites over 100 ps, free of finite-size contamination. Our method is model-agnostic and can be expected to enable the efficient investigation of nonequilibrium excitation dynamics in dissipative lattices displaying local interactions.

## II. SMALL POLARON LATTICE

The dispersive Holstein model offers a physically transparent description of small polaron formation and transport in many semiconductors displaying strong carrier-phonon interactions, including organic crystals,<sup>73</sup> polymers,<sup>74</sup> and nanomaterials.<sup>75</sup> This model describes the migration of charge carriers (electrons or holes) or excitons that interact with their environment, influencing local lattice (nuclear) motions. This interaction causes the material to deform around the carrier, forming a *polaron*.

In the dispersive Holstein model,

$$\hat{H} = \hat{H}_s + \hat{H}_{ph} + \hat{H}_{s-ph}, \quad (1)$$

where  $\hat{H}_s$  describes the electronic carriers:

$$\hat{H}_s = \sum_i^N \epsilon_i \hat{a}_i^\dagger \hat{a}_i + \sum_{\langle ij \rangle} v_{ij} \hat{a}_i^\dagger \hat{a}_j. \quad (2)$$

Here  $\epsilon_i$  represents the on-site energy,  $v_{ij}$  the hopping integral connecting the  $i^{\text{th}}$  and  $j^{\text{th}}$  sites,  $N$  the number of sites on the lattice, and  $\langle ij \rangle$  restricts the sum to nearest neighbor coupling. While a carrier couples to a single local phonon mode per lattice site in the classic Holstein model,<sup>1,2,76</sup> we opt for the dispersive version where a carrier couples to a continuum of local phonon modes, which more faithfully represents condensed phase systems<sup>77-80</sup> and has a full harmonic phonon environment per lattice site,

$$\hat{H}_{ph} = \frac{1}{2} \sum_i \sum_\alpha [\hat{P}_{i,\alpha}^2 + \omega_{i\alpha}^2 \hat{X}_{i,\alpha}^2]. \quad (3)$$

$\hat{X}_{i,\alpha}$  and  $\hat{P}_{i,\alpha}$  are mass-weighted positions and momenta for the  $\alpha^{\text{th}}$  phonon connected to the carrier on site  $i$ .

The carrier-phonon coupling is linear in the phonon coordinates,

$$\hat{H}_{s-ph} = \sum_i \sum_\alpha c_{i,\alpha} \hat{X}_{i,\alpha} \hat{a}_i^\dagger \hat{a}_i. \quad (4)$$

This carrier-phonon coupling is fully characterized by the spectral density  $J_i(\omega) = \frac{\pi}{2} \sum_\alpha \frac{c_{i,\alpha}^2}{\omega_{i\alpha}} \delta(\omega - \omega_{i\alpha})$ .

Consistent with previous works,<sup>5,41,71</sup> we focus on the dilute limit (one-carrier manifold) of homogeneous lattices, making all our parameters site-independent. Without loss of generality, we set  $\epsilon_i = 0$ , nearest-neighbor hopping integral  $v_{ij} = v$ , intersite distances  $r_0 = 5 \text{ \AA}$ , and all spectral densities to an Ohmic-Debye form commonly used to mimic dissipation in the condensed phase:<sup>81</sup>  $J(\omega) = \eta \omega_c \omega / (\omega^2 + \omega_c^2)$ . Here,  $\eta/2$  is the lattice reorganization energy of an occupied lattice site, and  $1/\omega_c$  the phonon environment's decorrelation time.

In our simulations, we track the population matrix  $\mathbf{C}(t)$ , where  $C_{i,j}(t) = \text{Tr}[\hat{a}_i^\dagger \hat{a}_i e^{-i\mathcal{L}t} \hat{\rho}_j(0)]$  with initial condition  $\hat{\rho}_j(0) = \hat{a}_j^\dagger \hat{a}_j e^{-\beta \hat{H}_{ph}} / \text{Tr}[e^{-\beta \hat{H}_{ph}}]$ , which corresponds to creating an excitation at site  $j$  at  $t = 0$  when all the phonon modes are in thermal equilibrium with the electronic ground state at inverse temperature  $\beta = 1/k_B T$ .  $C_{i,j}(t)$  quantifies the probability of finding the polaron at site  $i$  at time  $t$  given that it was initiated at site  $j$ . In homogeneous systems with equivalent sites and periodic boundary conditions,  $\mathbf{C}(t)$  exhibits translational invariance, i.e.,  $C_{i,i+l \bmod N}(t) = C_{j,j+l \bmod N}(t)$  for all  $i, j, l$ . This allows one to identify all distinct elements of this matrix by their relative site index,  $|i - j| = k$ , allowing one to rewrite  $C_{i,j}(t) = C_{|i-j|}(t) = C_k(t)$ . Hence, one only needs to perform a single simulation starting the carrier at any particular site,  $j$ , and record the time-dependent probability of finding the carrier at all lattice sites,  $i$ , as a function of time to construct  $\mathbf{C}(t)$ .

To characterize transport, we compute the polaron's mean squared displacement,  $MSD(t) = r_0^2 \sum_k k^2 C_k(t)$ , which determines its diffusion constant  $D$  via the time derivative when the  $MSD$  scales linearly in time:

$$D = \frac{1}{2N_d} \lim_{t \rightarrow \infty} \frac{dMSD}{dt}. \quad (5)$$

Here  $N_d$  indicates the lattice dimension. We calculate the reference  $\mathbf{C}(t)$  using the numerically exact Hierarchical Equation of Motion (HEOM)<sup>82-84</sup> under periodic boundary conditions at  $T = 300 \text{ K}$  for all simulations in this work (see App. A for additional details).

## III. METHOD DEVELOPMENT & ANALYSIS

We begin with the  $\frac{dMSD}{dt}$  dynamics of dispersive Holstein polarons on a 1D lattice. To align with previous work on organic semiconductors,<sup>41,85</sup> we take  $\eta = 323 \text{ cm}^{-1}$ ,  $v = 50 \text{ cm}^{-1}$  and  $\omega_c = 41 \text{ cm}^{-1}$ . Beyond encoding the diffusion constant,  $\frac{dMSD}{dt}$  provides insights

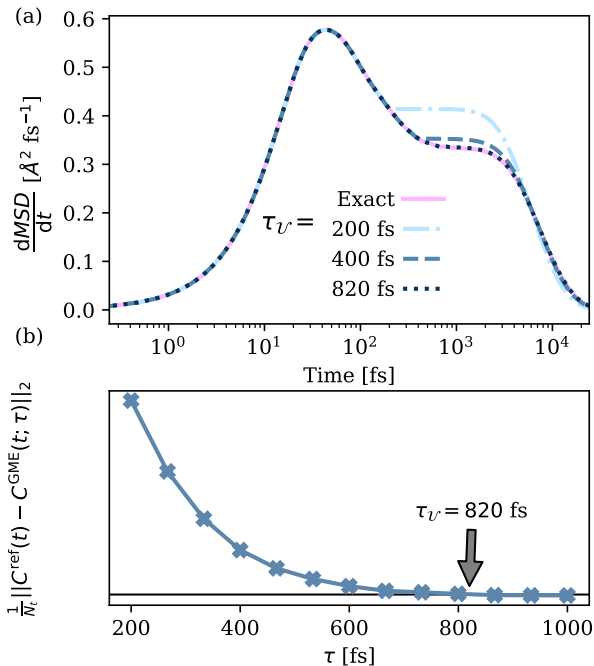


FIG. 1. Nonequilibrium polaron dynamics on a 20-site 1D lattice with  $\eta = 323 \text{ cm}^{-1}$ ,  $v = 50 \text{ cm}^{-1}$  and  $\omega_c = 41 \text{ cm}^{-1}$ . (a) Comparison of  $dMSD/dt$  between the exact (pink) and TL-GME dynamics generated with different lifetimes (broken blue lines). (b)  $\|L\|_2$  error for the TL-GME prediction as a function of the proposed time cutoff reveals  $\tau_U \approx 820 \text{ fs}$ . The error is normalized by the number of time points predicted by the GME,  $N_t$ .

into polaron formation, the transition from nonequilibrium relaxation to diffusive transport, and the onset of finite-size contamination.<sup>41</sup> For example, in the reference (HEOM) dynamics for the 20-site lattice (solid pink line) in Fig. 1 (a), the initial hump at  $\sim 100 \text{ fs}$  reports on far-from-equilibrium lattice reorganization from polaron formation, and is followed by a plateau that suggests diffusive motion between 800 and 2000 fs. While this region is not truly flat, it approximates the diffusion constant.<sup>41</sup> This putative plateau falls off at  $\sim 2000 \text{ fs}$ , marking the onset of finite-size effects. We denote this onset timescale as  $\tau_R$ .

We significantly reduce the computational cost of this simulation by adopting a GME for the population matrix. Specifically, we adopt the integrated time-local (TL) master equation<sup>59</sup> (see App. B):

$$\mathbf{C}(t + \delta t) = \mathbf{U}(t)\mathbf{C}(t), \quad (6)$$

where  $\mathbf{U}(t)$  is the generator of the non-Markovian dynamics for  $\mathbf{C}(t)$ . In dissipative lattice systems,  $\mathbf{U}$  can be expected to have a finite memory lifetime  $\tau_U$ , after which it becomes a time-independent matrix  $\mathbf{U}(\tau_U)$ , indicating the onset of Markovianity. At this point, Eq. 6 simplifies to a time-independent rate equation and one can efficiently generate long-time dynamics through matrix multiplication:

$$\mathbf{C}(\tau_U + n\delta t) = [\mathbf{U}(\tau_U)]^n \mathbf{C}(\tau_U), \quad (7)$$

where  $n \in \mathbb{N}$ . We use the reference HEOM dynamics to calculate the generator using

$$\mathbf{U}(t) = \mathbf{C}(t + \delta t)[\mathbf{C}(t)]^{-1}. \quad (8)$$

To identify the generator lifetime,<sup>59</sup> we truncate  $\mathbf{U}(t)$  at sample lifetimes  $\tau$  and use the resulting generator to produce TL-GME dynamics, from which we compute the  $\|L\|_2$  norm of the difference between the reference dynamics and the TL-GME dynamics. We find that  $\tau_U = 820 \text{ fs}$ , which is when the error metric in Fig 1 (b) plateaus near zero, allowing the resulting TL-GME dynamics (dotted blue line) to agree with the reference dynamics (pink line) in Fig 1 (a). Employing a smaller lifetime for the generator causes the TL-GME to predict inaccurate dynamics, as illustrated by the dashed blue lines in Fig. 1 (a). Hence, one only needs a reference simulation up to the generator lifetime  $\tau_U = 820 \text{ fs}$  to generate the dynamics over 25 ps—more than an order of magnitude longer—via simple matrix multiplication. Yet, while combining exact simulations with the TL-GME can reduce the computational cost of generating long-time dynamics in such lattice problems, the finite size of the lattice invariably poisons the dynamics once the polaron reaches the boundary. This prompts us to ask: can one reach large system sizes without incurring the cost of reference simulations over increasingly larger lattices that become prohibitively expensive?

**Spatial memory:** We address this fundamental problem by leveraging the concept of *spatial memory* to develop a *space-local (SL)* GME that uses only a short-time simulation of a small lattice to predict the dynamics of thermodynamically large lattices over arbitrary times. We begin by noting that, like  $\mathbf{C}(t)$ ,  $\mathbf{U}(t)$  exhibits translational invariance in homogeneous lattices, allowing us to use relative indices to identify the elements. Figure 2 (a) shows that as intersite distance increases, the elements of  $\mathbf{U}(t)$  become progressively smaller,  $U_{d+2} < U_{d+1} < U_d$ , suggesting that our TL-GME generator exhibits decaying spatial memory. Further, one may posit that generator elements connecting sites separated by a distance greater than a *characteristic memory distance*,  $d_U$ , become negligibly small, allowing one to set them to zero. We illustrate this concept of spatial memory truncation in Fig. 2 (b), where we discard the elements of  $\mathbf{U}(t)$  beyond a particular distance,  $d = d_U$ , as they become negligibly small.

We turn to testing the validity of SL-GME. We begin by examining the  $\|L\|_2$  error metric for the SL-GME as a function of the proposed memory distance cutoff,  $d$ , to identify the characteristic memory distance,  $d_U$ . Figure 3 (a) shows that the SL-GME reproduces the reference dynamics (solid pink line) when  $d_U = 3r_0$  (dotted brown line), but not for smaller cutoff distances. The plateau in the error as a function of distance cutoff in Fig. 3 (b) confirms that  $d_U = 3r_0$ , achieving an average error of less than 1%. These results thus support the proposal of a memory distance cutoff that preserves accuracy in the SL-GME dynamics.

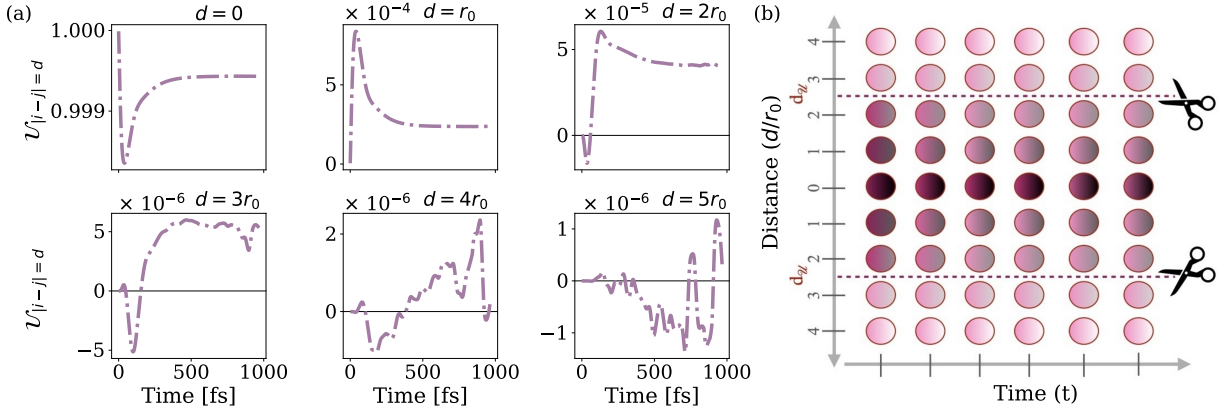


FIG. 2. (a) Elements of  $\mathbf{U}(t)$  as a function of lattice distance  $d$  for the dispersive Holstein lattice with the same parameters as Fig. 1. As inter-site distance,  $d$ , increases, the elements of  $\mathbf{U}(t)$  become smaller. (b) Schematic representation of the spatial locality in the generator,  $\mathbf{U}(t)$ , where elements beyond a characteristic distance  $d_U$  become negligible. The color intensity quantifies the magnitude of the elements and the scissors indicate the spatial truncation of the generator.

Since obtaining the generator up to its lifetime  $\tau_U$  allows one to simulate the dynamics for *all time*, one may hypothesize that constructing the generator up to its characteristic memory distance  $d_U$  should enable one to simulate a lattice of *any size*, albeit of the same dimension. This is the central insight of our *space- and time-local GME (STL-GME)*. To achieve this in a 1D

lattice, we propose *augmenting* the dimension of  $\mathbf{U}(t)$ , which is a 3-tensor with dimensions  $[N, N, tsteps]$ , to  $[M, M, tsteps]$ , where  $M > N$  and all new elements are assigned a value of 0. Further truncating the temporal dimension of our augmented generator at time  $\tau_U$  enables us to easily generate the dynamics after  $\tau_U$  via simple matrix multiplication. This spatial and temporal truncation of  $\mathbf{U}(t)$  followed by its spatial augmentation constitutes our STL-GME. We offer details of its implementation in App. C. The resulting STL-GME should thus offer a route to employ the dynamics of a small lattice over short times to simulate the behavior of a thermodynamically large lattice across arbitrarily long timescales.

We test our STL-GME's performance by turning again to the Holstein lattice in Figs. 1 and 3. Since  $\mathbf{U}$  is an *intrinsic* property of the dynamics, one can extract it from short-time  $t \leq \tau_U$  reference dynamics of a lattice with  $N \geq 2d_U + 1$  sites. One can then employ  $\mathbf{U}(t)$  to predict relaxation dynamics over *arbitrarily large spaces and times, removing all finite-size artifacts*. We validate this idea in Fig. 4, where we construct the generator for our STL-GME dynamics for a lattice with  $N = 20$  sites using a reference simulation of a lattice with only  $N = 8 > 2 \times (d_U = 3) + 1$  sites (solid purple line). Our size-augmented STL-GME in Fig. 4 (light purple dots) reproduces the reference dynamics for a lattice with  $N = 20$  sites (solid pink line). In fact, the STL-GME can access the dynamics of arbitrarily large systems, indefinitely delaying the onset of finite-size effects. As we show in the inset of Fig. 4, a 20-site lattice exhibits finite-size artifacts around  $\sim 2000$  fs, whereas our STL-GME calculation for the 100-site system shows no signs of finite-size effects, even by 25 ps.

Yet, that  $N$  can be so small in the reference calculation used to construct the generator in Fig. 4 is surprising. Here,  $\tau_U \simeq 800$  fs, but for an 8-site lattice, finite-size effects manifest in  $dMSD/dt$  at  $\sim 300$  fs, i.e.,  $\tau_R \simeq 300$  fs. However, despite  $\tau_U > \tau_R$ , the STL-GME and reference

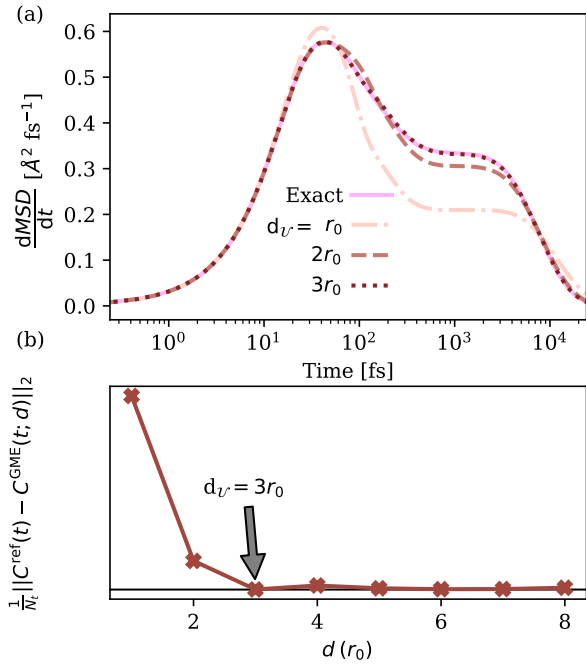


FIG. 3. Demonstration of the SL-GME's ability to capture the polaron dynamics on the 20-site 1D lattice with the same parameters as Fig. 1. (a) Comparison of  $dMSD/dt$  dynamics obtained with exact HEOM (pink solid line) and SL-GME (brown broken lines) dynamics. (b) Deviation (error) of the SL-GME dynamics from the exact dynamics as a function of distance cutoff, revealing that  $d_U = 3r_0$ . Error is defined in the same way as of Fig. 1 (b)

calculations agree, meaning the STL-GME correctly simulates the larger lattice and is not contaminated by the smallness of the reference system.

How can one understand this seeming contradiction where the generator lifetime,  $\tau_U$ , can be longer than  $\tau_R$ , the onset of finite-size effects in  $dMSD/dt$ ? Immediately at  $\tau_R$ , the finite-size effect contaminates only the elements of  $\mathbf{U}$  connecting the origin to the most distant sites. This is true because the population density is conserved and its current local. In time, this artifact spreads to elements of  $\mathbf{U}$  progressively closer to the origin, as the density interferes with itself. One might hypothesize that finite-size effects only manifest in the STL-GME when the elements of  $\mathbf{U}$  that survive the spatial truncation have been contaminated—a time longer than  $\tau_R$ .

To confirm this hypothesis, in Fig. 5 we compare the STL-GME generator and dynamics constructed from reference data for two different lattice sizes with varying cutoff distances. The parameter regime is the same as in Fig. 4, where we found  $d_U = 3r_0$  and  $\tau_R = 300$  fs, thus requiring a minimal lattice of  $N = 8$ . Keeping  $\tau_U = 800$  fs constant, we consider two complementary cases. First, for a too-small 6-site lattice, we know that obtaining a result free of finite-size effects is impossible because the periodic boundary is always closer than 3 sites from the initial polaron position. Indeed,  $\mathcal{U}_{N=6}(d = 3r_0, t)$  differs significantly from the benchmark  $\mathcal{U}_{N=20}(d = 3r_0, t)$  (Fig. 5 (a)), with the former producing STL-GME dynamics that deviate from the reference simulation for a

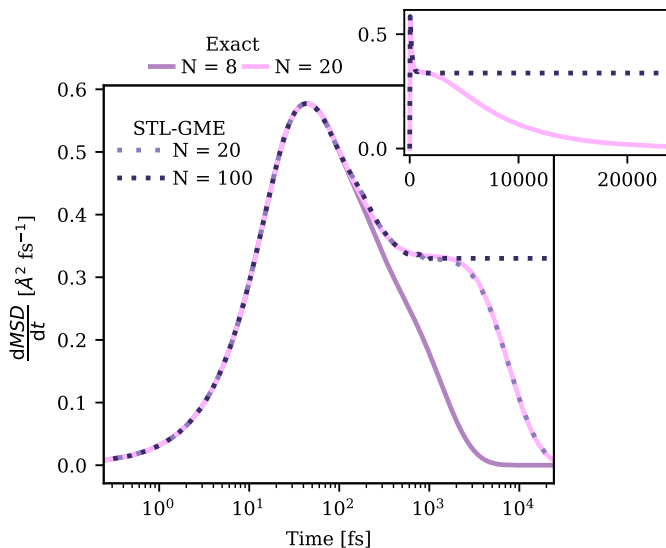


FIG. 4. Benchmarking of our STL-GME for dispersive Holstein dynamics for a 20-site (pink line) 1D lattice with  $\eta = 323$   $\text{cm}^{-1}$ ,  $v = 50$   $\text{cm}^{-1}$ ,  $\omega_c = 41$   $\text{cm}^{-1}$ . We construct our STL-GME generator using a reference 8-site (purple line) simulation, which we then augment in size to simulate GME dynamics for 20- and 100-site lattices (broken blue lines). Inset: normal-scale plot of  $dMSD/dt$  for the 20- and 100-site lattices. The 20-site dynamics exhibit finite-size effects around  $\sim 2000$  fs, while the 100-site lattice does not manifest them over the simulated times.

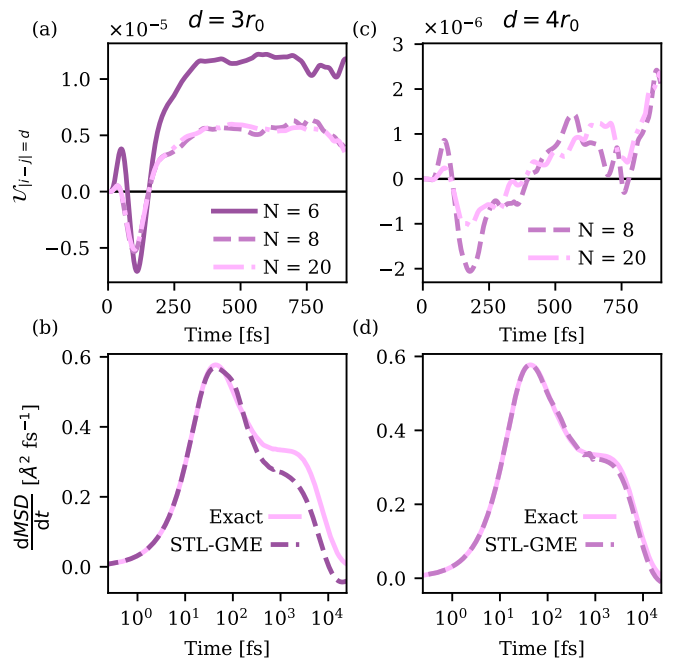


FIG. 5. Convergence of generator elements as a function of lattice size and characteristic memory distance,  $d_U$ , for dispersive Holstein parameters  $v = 50$   $\text{cm}^{-1}$ ,  $\eta = 323$   $\text{cm}^{-1}$ ,  $\omega_c = 41$   $\text{cm}^{-1}$ . (a)  $\mathcal{U}(d = 3r_0, t)$  as a function of lattice size. (b) Impact of adopting a generator from a too-small lattice,  $\mathcal{U}_{N=6}(d = 3r_0, t)$ . (c)  $\mathcal{U}(d = 4r_0, t)$  as a function of lattice size. (d) Impact of adopting a (contaminated) generator from a too-large choice of cutoff distance for the lattice size,  $\mathcal{U}_{N=8}(d = 4r_0, t)$ .

20-site lattice (Fig. 5 (b)). Second, we consider the previously sufficient 8-site lattice, but increase the cutoff to  $d_U = 4r_0$ . Since  $N < 2d_U + 1$ , we predict finite-size contamination in  $\mathcal{U}_{N=8}(d = 4r_0, t)$ . This is evident when comparing with the benchmark  $\mathcal{U}_{N=20}(d = 4r_0, t)$  (Fig. 5 (c)) and from the STL-GME dynamics, which again deviate from the reference (Fig. 5 (d)). That is, while the 8-site lattice generator's first 4 entries are correct for this  $\tau_U$ , the fifth element is contaminated by finite-size artifacts, degrading the predicted dynamics. In both of these pathological cases, truncation in time and space happens *after* knowledge of the lattice's finite size reaches those elements in  $\mathbf{U}$  that we keep. Therefore, a lattice with  $N = 8$  sites converges to the right value when one truncates spatially at  $d_U = 3r_0$ , as we confirm by comparing  $\mathcal{U}_{N=8}(d = 3r_0, t)$  and  $\mathcal{U}_{N=20}(d = 3r_0, t)$ , and the resulting STL-GME prediction with the reference results for a 20-site lattice, shown in Fig. 4. Hence, the STL-GME is even more efficient in accessing the dynamics of thermodynamically large systems from small reference calculations than one might have expected based on simple physical arguments.

**Applicability:** Thus far, we have assumed only nearest-neighbor coupling, raising questions about the extent to which our conclusions depend on the locality of the Hamiltonian. For example, if the electronic coupling

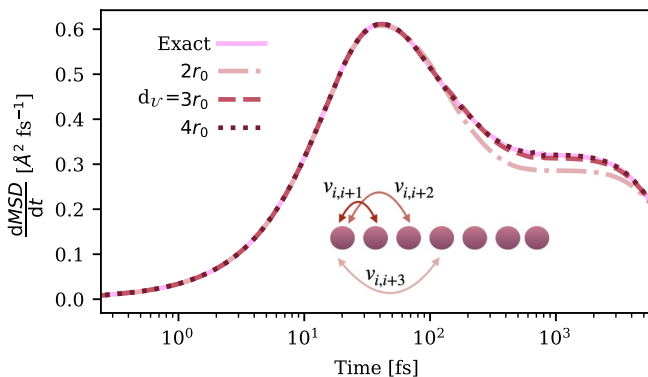


FIG. 6. Applicability of the STL-GME for a dispersive Holstein lattice with short-range, non-local couplings. Hamiltonian parameters:  $\eta = 323 \text{ cm}^{-1}$ ,  $v(r_0) = 50 \text{ cm}^{-1}$ ,  $v(2r_0) \approx 6.8 \text{ cm}^{-1}$ ,  $v(3r_0) \approx 1.0 \text{ cm}^{-1}$ ,  $\omega_c = 41 \text{ cm}^{-1}$ .

extends further, over second and third nearest neighbors, do the cutoffs extend by  $2r_0$ , or is there a more pernicious, qualitative change?

To probe this potential sensitivity to non-locality, we recalculate our dispersive Holstein dynamics with beyond-nearest-neighbor electronic couplings for the parameter regime of Fig. 3, where we had identified  $d_U = 3r_0$  when considering only nearest-neighbor coupling. Motivated by atomic orbital decays, we consider interactions that decrease exponentially with inter-site distance up to third nearest neighbors, as shown in Fig. 6, with  $v(d) = ve^{-a(d-r_0)}$ ,  $a = 2r_0^{-1}$ . Even in this non-locally interacting problem, Fig. 6 shows that our STL-GME captures the reference dynamics with  $d_U = 4r_0$ . This change in cutoff distance of one lattice spacing is even less severe than the  $2r_0$  one may have anticipated. Thus, our STL-GME efficiently handles Hamiltonians with non-local, albeit short-range, interactions. While more general models include long-range, through-space effects like carrier-carrier interaction, screening in the condensed phase<sup>86–93</sup> usually allows for a truncation that can be modeled similarly to the modification tested here and should therefore preserve the space-local arguments central to our STL-GME method.

**Computational efficiency:** The major advantage of our STL-GME is the significant computational savings it offers. Specifically, exact numerical methods scale polynomially or exponentially with  $N$  and simulation time. In contrast, our STL-GME scales only as  $N^2$  with a prefactor that heavily suppresses the cost to keep it effectively constant (see Fig. 7) and (sub)linearly<sup>94</sup> in time. The main source of computational expense in our STL-GME arises from the short-time reference calculation on a small lattice needed to construct the generator. Figure 7 compares the computational cost of HEOM and the STL-GME built from a small reference calculation as a function of  $N$ . We fit the time costs for HEOM with a polynomial regression (gray dashed line in Fig. 7). Even with our highly optimized implementation of HEOM that exploits recent advances in dynamic filtering of auxiliary density matrices<sup>82</sup> and the  $n$ -particle approximation,<sup>84</sup>

the direct simulation for a 100-site lattice over 25 fs is  $\sim 300$  times more computationally expensive than our STL-GME for the same parameter regime. We can further extend the 100-site lattice’s dynamics to arbitrarily long times using our STL-GME for the trivial cost of repeated small matrix multiplications. This STL-GME-enabled simulation allows us to find that finite-size effects emerge at  $\sim 65$  ps for the 100-site lattice—a timescale that is currently unreachable for a system of this size with a direct HEOM simulation. Such a calculation would require at least 10,500 CPU hours (optimistically assuming a linear relationship between simulation time and CPU time), making it 750 times more computationally costly than our STL-GME. Instead, with our STL-GME, the same 100-site simulation requires effectively the same amount of time as an 820 fs-long simulation for an 8-site lattice (13.5 CPU hours), as we can compute the STL-GME dynamics in *less than a minute*.

**2D polaron transport:** Our STL-GME method can easily generalize to higher-dimensional lattices. This enables us to access, for the first time, the exact quantum dynamics of polaron formation and transport in dimensions above one. Accessing transport in 2D is particularly significant as it yields the spatiotemporal spread of polarons on a surface—a phenomenon that recent microscopy experiments measure.<sup>95–102</sup> Such simulations can elucidate the microscopic factors that influence energy and charge flow in materials and offer insights on how to modify them for specific applications, such as energy storage or battery development.<sup>103–106</sup>

For our demonstration, we select Hamiltonian parameters characterized by high reorganization energy relative to the hopping integral and a fast phonon decorrelation speed, appropriate for polarons in organic crystals.<sup>107</sup> To interrogate the effect of various energy scales on polaron transport, we examine a homogeneous 2D lattice characterized by two types of hopping integrals that

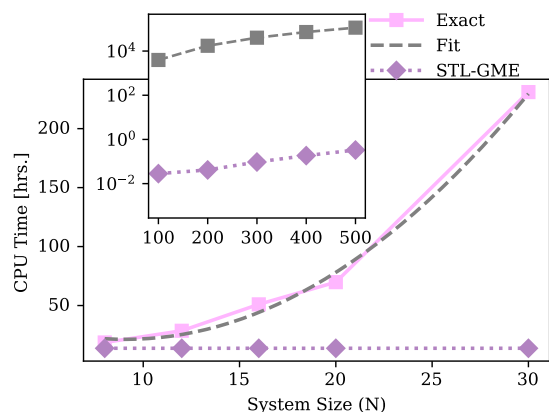


FIG. 7. Comparison of computational resources (CPU time) needed to reach 25 ps of simulation time using a direct HEOM simulation versus our STL-GME-enabled simulation. Inset: log scale plot of computational time requirement for the STL-GME extension and (extrapolated fit to) exact simulation for large  $N$ .

can cause anisotropic flow,  $\mathcal{V}_\perp$  and  $\mathcal{V}_\parallel$ , as illustrated in Fig. 8 (a). Figure 8 (b)-(d) illustrates the polaron motion on a  $30 \times 30$ -site 2D lattice with a total of 900 sites. Such a large-scale simulation is made possible exclusively through our STL-GME method (see App. D for implementation details).

We turn to the effect of varying  $\mathcal{V}_\perp$  relative to  $\mathcal{V}_\parallel$ . Unsurprisingly, when  $\mathcal{V}_\perp = \mathcal{V}_\parallel$ , we observe a symmetric spread of the polaron at  $t = 10$  ps, as shown in Fig. 8 (b). Anisotropic motion can be expected to emerge when  $\mathcal{V}_\perp \neq \mathcal{V}_\parallel$ . Indeed, when  $\mathcal{V}_\perp = 2\mathcal{V}_\parallel$  and  $\mathcal{V}_\perp = 4\mathcal{V}_\parallel$ , polaron density spreads more rapidly along the vertical axis, as shown in Figs. 8 (c) and (d), respectively, with the ratio  $\mathcal{V}_\perp/\mathcal{V}_\parallel$  dictating the anisotropy of the polaron distribution on the 2D surface. This demonstrates that STL-GME can efficiently simulate nonequilibrium polaron motion in higher-dimensional systems, even in the thermodynamic limit. Hence, this framework offers an accurate and efficient means to simulate polaron transport over the length and time scales needed to compare to experiments.

**Time nonlocal formulation:** Our space locality arguments are also compatible with the time-nonlocal description of memory.<sup>62–64</sup> In App. E, we formulate the space-local time-nonlocal (SL-TNL) GME, where we further unify the SL framework with the Transfer Tensor Method.<sup>108</sup> Interestingly, we find that the time-local characteristic memory distance,  $d_{\mathcal{U}}$ , is shorter than its time-nonlocal counterpart,  $d_{\mathcal{K}}$ . We also find that the generator and memory kernel lifetimes in the time-local and time-nonlocal formulations follow a similar inequality,

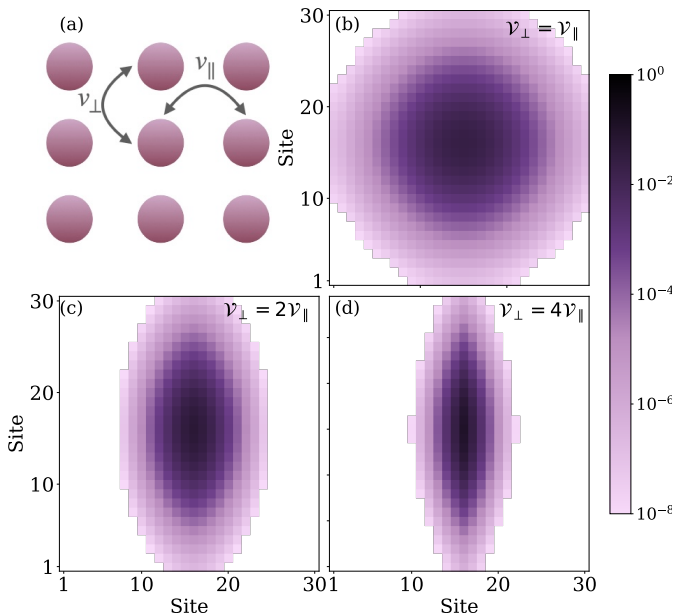


FIG. 8. Polaron density in a  $30 \times 30$ -site lattice with dispersive Holstein parameters  $\eta = 500 \text{ cm}^{-1}$ ,  $v = 25 \text{ cm}^{-1}$  and  $\omega_c = 41 \text{ cm}^{-1}$ . (a) Schematic of a 2D lattice with two types of hopping integrals:  $\mathcal{V}_\perp$  and  $\mathcal{V}_\parallel$ . Polaron density at  $t = 10$  ps for three cases: (b)  $\mathcal{V}_\perp = \mathcal{V}_\parallel = v$ ; (c)  $\mathcal{V}_\perp = 2v$  and  $\mathcal{V}_\parallel = v$ ; and (d)  $\mathcal{V}_\perp = 4v$  and  $\mathcal{V}_\parallel = v$ .

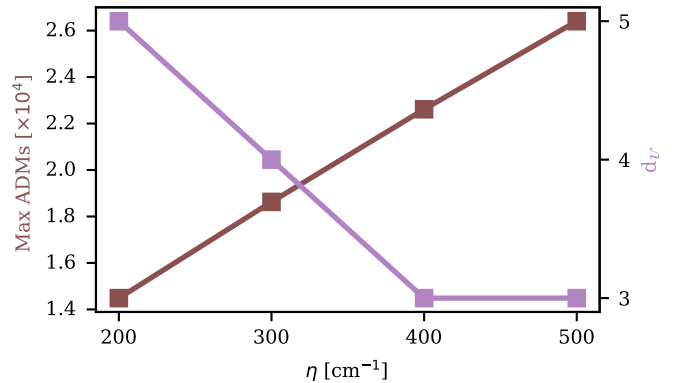


FIG. 9. The computational cost of HEOM (solid brown line) rises with growing electronic-phonon coupling ( $\eta$ ) while the cutoff (and therefore cost) decreases for our STL-GME (solid purple line). Hamiltonian parameters:  $v = 50 \text{ cm}^{-1}$ ,  $\omega_c = 100 \text{ cm}^{-1}$ .

ity,  $\tau_{\mathcal{U}} \leq \tau_{\mathcal{K}}$ , consistent with our previous findings in biomolecular dynamics.<sup>68</sup>

**Entanglement:** For systems involving coupling between spins or fermions with phonons, increasing the reorganization energy leads to high electronic-nuclear entanglement. This generally translates into greater computational cost for many numerically exact<sup>11–14,16</sup> and approximate dynamics methods.<sup>109–111</sup> For instance, the number of differential equations that must be propagated at each step in HEOM grows significantly with increasing reorganization energy, raising its computational cost. Similarly, in matrix product state-based propagation schemes, the bond dimension increases with increasing reorganization energy and simulation time,<sup>22,26</sup> further escalating computational demands. In contrast, in our SL-GME approach, increasing reorganization energy *reduces*  $d_{\mathcal{U}}$  (see Fig. 9). This allows us to perform reference calculations on smaller lattices, providing dramatic computational savings in systems with large reorganization energies.

#### IV. CONCLUSION

While it is well-known that the temporal truncation of memory in traditional GMEs can significantly lower the computational cost of dynamic simulations *over arbitrary times*, here we introduce space-local GMEs where spatial truncation of memory can dramatically lower the cost of accessing the dynamics of complex many-body systems *of arbitrary sizes*. By integrating both spatial and temporal truncation in the same GME framework within a time-local framework, we have developed a novel STL-GME that allows us to leverage the dynamics of small lattices over short times to exactly simulate the dynamics of thermodynamically large systems across arbitrary times, free from finite-size effects. In addition to our time-local formulation, we have developed analogous continuous and discrete time-nonlocal GMEs.

We have demonstrated the benefits offered by our STL-

GME when simulating polaron formation and transport in dispersive Holstein lattices in 1D and 2D with short-range couplings. In fact, our STL-GME has already revealed that nonequilibrium lattice relaxation can exponentially delay the onset of polaron diffusion.<sup>112</sup> Our approach, however, can be expected to find applications across a wide range of dissipative lattice problems to interrogate the nonequilibrium relaxation dynamics of charge, electronic energy, and heat flow. We have shown, for example, that our SL-GMEs are broadly compatible with systems displaying short-range interactions and in arbitrary dimensions. In addition, like previous GMEs, our SL-GMEs are agnostic to the choice of dynamics solver (classical or quantum, exact or approximate) used to construct the time-local generator or memory kernel, broadening its applicability to a wide variety of systems and phenomena. By offering access to experimentally relevant nonequilibrium relaxation processes in thermodynamically large systems over arbitrarily long times, our STL-GME can be expected to provide a transformative tool to uncover and explain new dynamical phenomena in periodic materials.

## ACKNOWLEDGEMENTS

Acknowledgment is made to the donors of the American Chemical Society Petroleum Research Fund for partial support of this research (No. PRF 66836-DNI6). A.M.C. acknowledges the support from a David and Lucile Packard Fellowship for Science and Engineering. S.B. acknowledges the John Bailar Memorial Endowment and the Marion L. Sharrah Fellowship for partial support of the research. T.S. is the recipient of an Early Career Fellowship from the Leverhulme Trust. We thank Prof. Qiang Shi for sharing his HEOM code with us. This work utilized the Alpine high-performance computing resource at the University of Colorado Boulder. Alpine is jointly funded by the University of Colorado Boulder, the University of Colorado Anschutz, Colorado State University, and the National Science Foundation (award 2201538).

## DATA ACCESSIBILITY

The data supporting our study's findings are available from the corresponding author upon reasonable request.

## Appendix A: HEOM simulations

HEOM<sup>11</sup> is a numerically exact method that predicts the dynamics of the reduced density matrix of an open quantum system by mapping environmental degrees of freedom to auxiliary density matrices (ADMs) that quantify the number of coupled differential equations being solved simultaneously. The reduced density matrix provides information about the polaron population.

We converge all HEOM calculations with respect to the hierarchical depth  $L$ , the number of Matsubara frequencies  $K$ , and the time step  $\delta t$ . For our 1D simulations,  $L = 22$ ,  $K = 1$ , and  $\delta t = 0.25$  fs. When changing reorganization energy for Fig. 9, we use  $L = 26$ ,  $K = 2$ , and  $\delta t = 0.25$  fs. Due to the extreme computational cost, we employed a high-temperature approximation for 2D simulations, setting  $K = 0$ , and converged the hierarchical depth and timestep to  $L = 26$  and  $\delta t = 0.25$  fs. In all our simulations, we apply dynamic filtering,<sup>82</sup> using a threshold of  $N_{\text{cut}} = 10^{-7}$  atomic units, in line with previous work.<sup>41,71</sup> We also employ  $n$ -particle approximation<sup>84</sup> to minimize numerical costs without affecting the accuracy of the results.

## Appendix B: GME Formulation

At the heart of GMEs is the projection operator,<sup>113</sup>  $\mathcal{P}$ , which enables one to derive the GME and establish the form of the correlation function of interest. Because we are interested in tracking the population matrix, we choose the nonequilibrium population projector<sup>51,114</sup>  $\mathcal{P} = |\mathbf{A}\rangle\langle\mathbf{A}| = \sum_{j=1}^N |A_j\rangle\langle A_j|$ , where  $A_j = \hat{a}_j^\dagger \hat{a}_j$  is the operator tracking fermionic occupation of site  $j$ . As in previous work,<sup>51</sup> we define the inner product as

$$\langle A_i | \hat{\mathcal{O}} | A_j \rangle = \frac{1}{Z_{\text{ph}}} \text{Tr} \left[ A_i^\dagger \hat{\mathcal{O}} A_j e^{-\beta \hat{H}_{\text{ph}}} \right], \quad (\text{B1})$$

where  $\hat{\mathcal{O}}$  is a superoperator and  $Z_{\text{ph}}$  is the partition function of the phonon modes. With this choice of projection operator, we can obtain the population correlation matrix  $\mathbf{C}(t)$  as follows

$$\mathbf{C}(t) = \langle \mathbf{A} | e^{-i\mathcal{L}t} | \mathbf{A} \rangle, \quad (\text{B2})$$

where  $\mathbf{C}(0) = \mathbf{1}$ . Here,  $e^{-i\mathcal{L}t}$  is the propagator that evolves an initial density in time, and  $\mathcal{L} = [H, \dots]$  is the Liouvillian operator. The  $i, j$  element of this correlation function takes the form

$$\begin{aligned} C_{i,j}(t) &= \frac{1}{Z_{\text{ph}}} \text{Tr} \left[ A_i^\dagger e^{-i\mathcal{L}t} A_j e^{-\beta \hat{H}_{\text{ph}}} \right] \\ &= \text{Tr} \left[ \hat{a}_i^\dagger \hat{a}_i e^{-i\mathcal{L}t} \hat{\rho}_j(0) \right]. \end{aligned} \quad (\text{B3})$$

We calculate  $\mathbf{C}(t)$  using HEOM.

## Appendix C: STL-GME for a 1D lattice

Here, we outline our protocol for building a size-augmented STL-GME for a 1D lattice using only a short-time simulation of a small lattice. Here we use HEOM to generate the reference dynamics, but our method is agnostic to the choice of solver.

1. Construct the generator  $\mathbf{U}(t)$  from the reference  $\mathbf{C}(t)$  using Eq. 8.



2. Identify the lifetime  $\tau_{\mathcal{U}}$  by computing the  $\|\mathbf{L}\|_2$  error between reference and GME-generated dynamics as a function of the proposed lifetime,  $\tau$ ,  $\text{Error}(\tau) = \frac{1}{N_t} \|\mathbf{C}^{\text{ref}}(t) - \mathbf{C}^{\text{GME}}(t; \tau)\|_2$ , and identify when the error function plateaus to a sufficiently low value.  $N_t$  represents the number of time points predicted by TL-GME, i.e., the number of time points used to construct the generator subtracted from the total number of time points in the reference dynamics. Our threshold per element of  $\mathbf{C}(t)$  is  $3 \times 10^{-8}$ .
3. Identify characteristic memory distance  $d_{\mathcal{U}}$  in a similar way by analyzing the error between reference dynamics and GME dynamics via the error as a function of the proposed cutoff distance,  $d$ ,  $\text{Error}(d) = \frac{1}{N_t} \|\mathbf{C}^{\text{ref}}(t) - \mathbf{C}^{\text{GME}}(t; d)\|_2$ . For SL-GME,  $N_t$  is the total number of points. Our threshold per element of  $\mathbf{C}(t)$  is  $6 \times 10^{-8}$ .
4. If one finds  $d_{\mathcal{U}} < N/2$ , this means reference simulation is sufficiently large for system size extension via generator augmentation. Keep the generator up to its lifetime  $\tau_{\mathcal{U}}$  only. Truncate the generator by setting its entries connecting sites with a relative distance  $d > d_{\mathcal{U}}$  to 0.
5. Augment the generator's dimension from  $[N, N, tsteps]$  to  $[M, M, tsteps]$ , where  $M$  is the length of the extended lattice. Then, populate all additional new entries in the matrix with 0.
6. Employ  $\mathbf{U}(t)[M, M]$  to propagate the dynamics. For time  $t \leq \tau_{\mathcal{U}}$ , use Eq. 6. For  $t > \tau_{\mathcal{U}}$ , use Eq. 7.

**Ensuring population conservation:** In our STL-GME method, we discard the elements of  $\mathbf{U}$  with relative lattice spacings larger than  $d_{\mathcal{U}}$  by setting them to 0. Our generator truncation—like singular value truncations in tensor network-based methods<sup>115</sup>—can cause violations of population conservation. We track this population loss via  $\sigma(t) = |1 - \sum_k C_k(t)|$ . Ideally,  $\sigma(t)$  should be as close to zero as possible. Figure 10 (a)—which corresponds to the parameter regime of Fig. 4 where we employ an 8-site reference simulation to predict the dynamics of a 20-site lattice—reveals that our spatial truncation causes a 1% population loss over the first 1 ps, which will continue to grow with simulation time.

To conserve the population, we propose two schemes:

1. *Redistribution:* Add all discarded elements and distribute them equally among all remaining elements of  $\mathbf{U}$  after truncation,

$$\mathcal{U}[i, j; d < d_{\mathcal{U}}] = \mathcal{U}[i, j; d < d_{\mathcal{U}}] + \frac{1}{N_{d_{\mathcal{U}}}} \sum_j \mathcal{U}[i, j; d > d_{\mathcal{U}}], \quad \forall i, \quad (\text{C1})$$

where  $N_{d_{\mathcal{U}}}$  is the number of elements in  $\mathcal{U}$  that we keep as nonzero entries in our generator after spatial truncation.

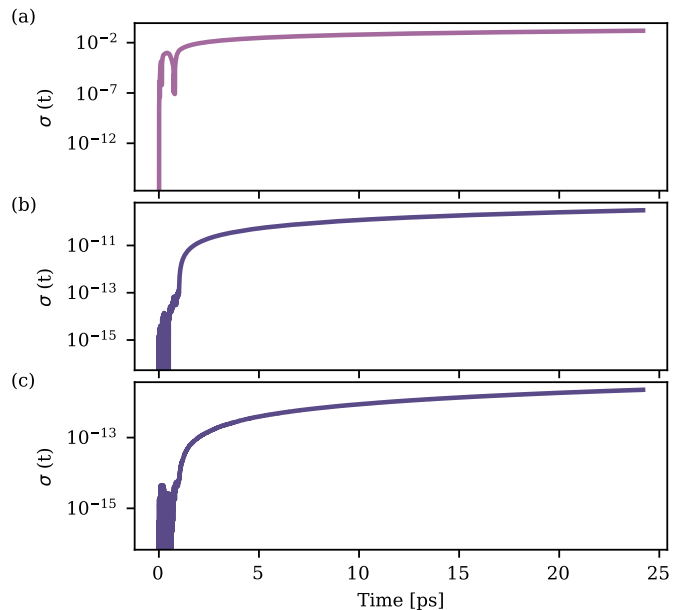


FIG. 10. Population loss  $\sigma(t)$  due to spatial truncation of the generator elements for the STL-GME dynamics for a 20-site lattice built from a reference 8-site simulation, as shown in Fig. 4. Population loss as a function of simulation time arising from: (a) performing a direct truncation of the generator; (b) adopting the redistribution scheme; (c) adopting the renormalization scheme

2. *Renormalization:* After spatial truncation, renormalize the generator  $\mathbf{U}$  matrix at each time step,

$$\mathcal{U}[i, j; d < d_{\mathcal{U}}] = \frac{\mathcal{U}[i, j; d < d_{\mathcal{U}}]}{\sum_j \mathcal{U}[i, j; d < d_{\mathcal{U}}]}, \quad \forall i. \quad (\text{C2})$$

Figure 10 shows when we add our population conservation schemes by redistributing or renormalizing spatially truncating generator  $\mathbf{U}$  we can keep the population loss in the order of  $10^{-11}$  and  $10^{-12}$ , even for longer simulation time. Figure 10 (b) and (c) shows the population loss quantity for redistribution and renormalization scheme respectively. In our study, we employ redistribution scheme for all 1D simulations and renormalization scheme for 2D simulations. While we show that we modify the generator to conserve the population, one could, in principle, imagine some level of modification in the population level to conserve the population.

**Managing finite numerical precision of the dynamical solver:** Figure 2 (a) shows that increasing lattice distance  $d$  makes the elements of the generator  $\mathbf{U}$  smaller. At some point, the size of these generator elements is commensurate with the statistical error or numerical precision error of the reference dynamical solver. While keeping the full generator intact ensures that the generator recovers the reference dynamics, truncating generator elements that may be at the level of the solver error can introduce small disagreements between the STL-GME and reference dynamics because of imperfect cancellation of error.

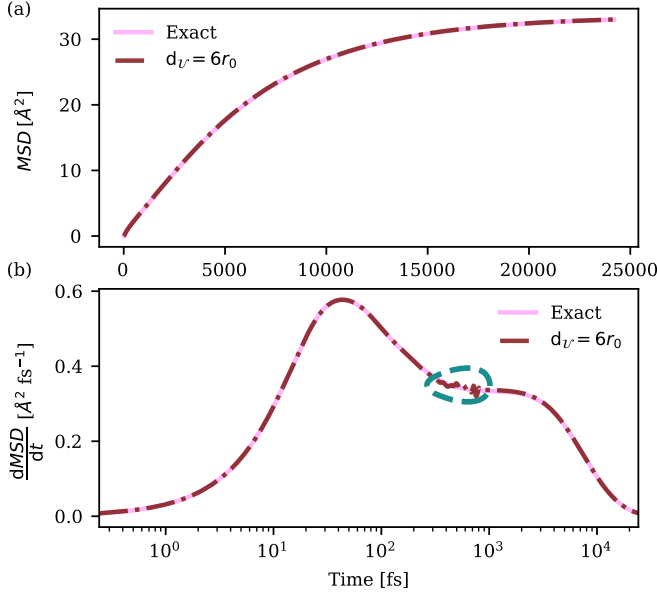


FIG. 11. (a) Comparison of  $MSD$  between exact result and STL-GME dynamics data for Fig. 3 parameters. Here we set a characteristic memory distance  $d_U = 6r_0$ . (b) Comparison of  $dMSD/dt$  between the exact result and the STL-GME dynamics with  $d_U = 6r_0$  for Fig. 3 parameters. The green encircled region between 400 fs and 1000 fs shows the inclusion of noise in the STL-GME dynamics.

To see how this finite precision error in the underlying solver can manifest in the STL-GME, consider generator elements connecting sites separated by inter-site distances of  $6r_0$  and  $7r_0$  in Fig. 12 (purple lines), which have contributions on the order of  $10^{-6}$  to  $10^{-7}$ . In our reference HEOM simulations, from which we build the generator, we use dynamic filtering with a threshold of  $N_{\text{cut}} = 10^{-7}$  atomic units. Including these small noisy elements in the truncated  $\mathcal{U}$  risks introducing noise into

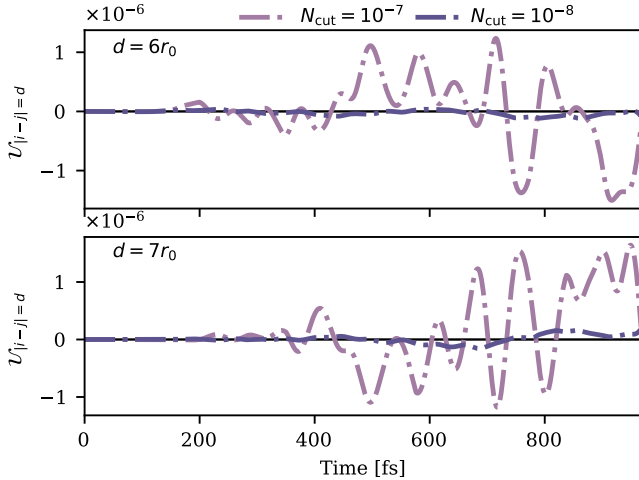


FIG. 12. Generator elements of  $\mathcal{U}$  for inter-site distances  $d = 6r_0$  and  $d = 7r_0$  for the parameters in Fig. 1 as a function of the strength of dynamic filtering in the HEOM solver,  $N_{\text{cut}}$ .

our dynamical quantities, with derivative quantities magnifying the effect of such noise. Specifically, when we choose  $d_U = 6r_0$  and compare the exact and STL-GME-predicted  $MSD$ , as shown in Fig. 11 (a), one cannot notice any visual difference. In contrast, when we compare the more sensitive  $dMSD/dt$ , we find a minor noisy behavior in the green-encircled region of Fig. 11 (b). This noise arises because elements in  $\mathcal{U}$  for  $d \geq 6r_0$  are discarded and set to 0, leading to insufficient noise cancellation from elements with  $d = 7r_0$  and beyond. Reducing this filter threshold to  $N_{\text{cut}}$  to  $10^{-8}$  decreases the noise in the  $6r_0$  and  $7r_0$  elements of  $\mathcal{U}$  (see Fig. 12). Hence, if smaller elements need to be included in the generator when implementing STL-GME, one must be mindful of the numerical precision of the underlying dynamical solver.

#### Appendix D: STL-GME for a 2D lattice

Here we summarize our modified protocol to build the STL-GME for a homogeneous 2D lattice. We note, however, that the same protocol can be used for an  $ND$  lattice with  $N \geq 2$ . To construct the input dynamical matrix,  $\mathcal{C}(t)$ , we perform a single reference HEOM simulation and then exploit translational symmetry. Once we construct  $\mathcal{C}(t)$ , we follow the following workflow to implement the STL-GME for a 2D lattice:

1. Compute the generator  $\mathcal{U}(t)$  from reference  $\mathcal{C}(t)$  using Eq. 8.
2. Identify the generator lifetime  $\tau_U$  by comparing the  $\|\mathcal{L}\|_2$  error between TL-GME results and reference dynamics.
3. Identify the spatial distance cutoff  $d_U$ :
  - (a) Keep the generator up to its lifetime,  $\mathcal{U}[N, N, t \leq \tau_U]$ .
  - (b) Reshape the first two lattice indices into  $x$  and  $y$  coordinate indices such that any lattice index  $a$  can be rewritten as
$$a = i \times N_x + j, \quad (\text{D1})$$
where  $N = N_x \times N_y$ . This transforms the generator into a 5-rank tensor:  $\mathcal{U}[N, N, t] \rightarrow \mathcal{U}[N_x, N_y; N_x, N_y, t]$ .
  - (c) To spatially truncate the generator for a homogeneous lattice:
    - i. Select an excitation starting at any lattice point, e.g., the origin of the 2D lattice,  $\mathcal{U}[N_x, N_y; 0, 0, t]$ .
    - ii. Compute the distance between this initial excitation at coordinates  $(0, 0)$  and any measurement site  $(i, j)$  as

$$d_{i,j} = \sqrt{i^2 + j^2} \quad \forall i, j. \quad (\text{D2})$$

- iii. Discard all the elements where  $d_{i,j} > d_{\mathcal{U}}$  by making them numerically 0.
  - iv. Apply Eq. C2 to this spatially truncated  $\mathcal{U}[N_x, N_y; 0, 0, t]$  to conserve the population.
  - v. Employ translational symmetry to populate full  $\mathcal{U}[N_x, N_y; N_x, N_y, t]$  from  $\mathcal{U}[N_x, N_y; 0, 0, t]$  by varying initial excitation lattice coordinates.
- (d) Collapse the coordinate indices into lattice indices using Eq. D1 such that  $\mathcal{U}[N_x, N_y; N_x, N_y, t] \rightarrow \mathcal{U}[N, N, t]$ .
- (e) Use the modified generator to propagate the dynamics using Eq. 6 (before  $t < \tau_{\mathcal{U}}$ ) and Eq. 7 after  $t < \tau_{\mathcal{U}}$ .
- (f) Calculate the  $\|\mathbb{L}\|_2$  error metric by comparing the exact dynamics with GME-predicted dynamics for different potential distance cutoffs to find  $d_{\mathcal{U}}$ .
4. If  $d_{\mathcal{U}} < N/2$ , the reference calculation is sufficiently large for spatial extension of the dynamics. To generate the dynamics of a system with extended size:
- (a) Augment the generator's dimension. Expand generator obtained from step (3c)  $\mathcal{U}[N_x, N_y; 0, 0, t]$  to  $\mathcal{U}[M_x, M_y; 0, 0, t]$  for all time points, where  $M_x \geq N_x$ ,  $M_y \geq N_y$  and  $M = M_x \times M_y$ , and assign 0 to all the new entries.
  - (b) Similar to step (3d), use translational symmetry to populate  $\mathcal{U}[M_x, M_y; M_x, M_y, t]$  for all initial conditions from  $\mathcal{U}[M_x, M_y; 0, 0, t]$  and collapse the coordinate indices to lattice indices, yielding the expanded generator,  $\mathcal{U}[M, M, t]$ , for the  $M \times M$  lattice system.
  - (c) Similar to step (4d), propagate the GME dynamics using  $\mathcal{U}[M, M, t]$  which predict population correlation matrix  $\mathbf{C}(t)$  for  $M \times M$  lattice.

For Figs. 8 (b)-(d), we simulate a  $8 \times 8$  lattice to obtain the reference  $\mathbf{C}(t)$  dynamics for the STL-GME extension. We find that the generator lifetime  $\tau_{\mathcal{U}} = 800$  fs and appropriate distance cutoff  $d_{\mathcal{U}} = 3r_0$ , suggesting that the  $8 \times 8$  lattice is sufficient as the reference simulation. We employ this  $8 \times 8$  dynamics to predict the dynamics of a  $10 \times 10$  lattice and confirm that our STL-GME dynamics agree with a separate exact HEOM simulation. In the main text (see Fig. 8 (b)-(d)), we employ our STL-GME protocol to augment the size to a  $30 \times 30$  lattice and simulate over the first 100 ps.

### Appendix E: Space-local time-nonlocal GME

Here we discuss the spatial locality of the memory kernel in the time-local GME and how to truncate small elements that become negligible with increasing inter-site

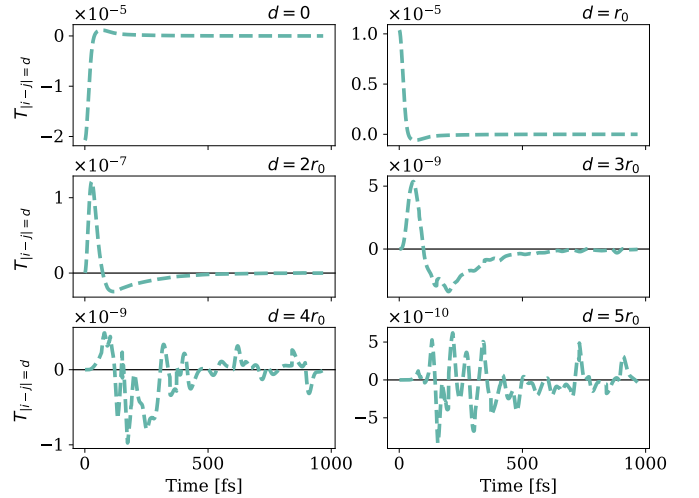


FIG. 13. Elements of the transfer tensor,  $\mathbf{T}(t)$ , as a function of intersite distance  $d$  for the dispersive Holstein lattice with the same parameters as Fig. 1.

distance. For lattice problems with short-range interactions and local couplings (such as the dispersive Holstein lattice), space-locality is also present in the time-nonlocal description of memory. We demonstrate space-locality in the Transfer Tensor Method (TTM), which is the discrete analog of the time-nonlocal GME.<sup>108</sup>

For the population projector, one can write the integrated time-nonlocal master equation via the TTM formulation,

$$\mathbf{C}(t) = \sum_k \mathbf{T}(t-k)\mathbf{C}(k), \quad (\text{E1})$$

where the memory kernel of the dynamics is encoded into the transfer tensor,  $\mathbf{T}(t)$ . We observe that the elements of the  $T_{i,j}(t)$  tensor become smaller with increasing lattice distance  $d$ , (see Fig. 13). Hence, we can spatially truncate  $\mathbf{T}(t)$  and then augment it to a larger dimension by adding zeroes to the new entries.

To demonstrate the performance of the SL-TNL-GME, we focus on the parameter regime of Fig. 1. Figure 14 (a) confirms that the SL-TNL-GME can recover the reference simulation. Figure 14 (b) shows that the characteristic memory distance in the time-nonlocal framework is  $d_{\mathcal{K}} = 5r_0$ , which is bigger than the analogous characteristic memory distance in the time-local framework,  $d_{\mathcal{U}} = 3r_0$ . Similarly, we find the memory kernel lifetime in the time-nonlocal formulation is  $\tau_{\mathcal{K}} = 850$  fs, which is bigger than the lifetime we identify in the time-local case,  $\tau_{\mathcal{U}} = 820$  fs. The latter result is consistent with previous findings in the context of biomolecular dynamics.<sup>68</sup> Hence, this example shows one can implement the idea of spatial memory truncation in the time-nonlocal formulation of reduced dynamics.

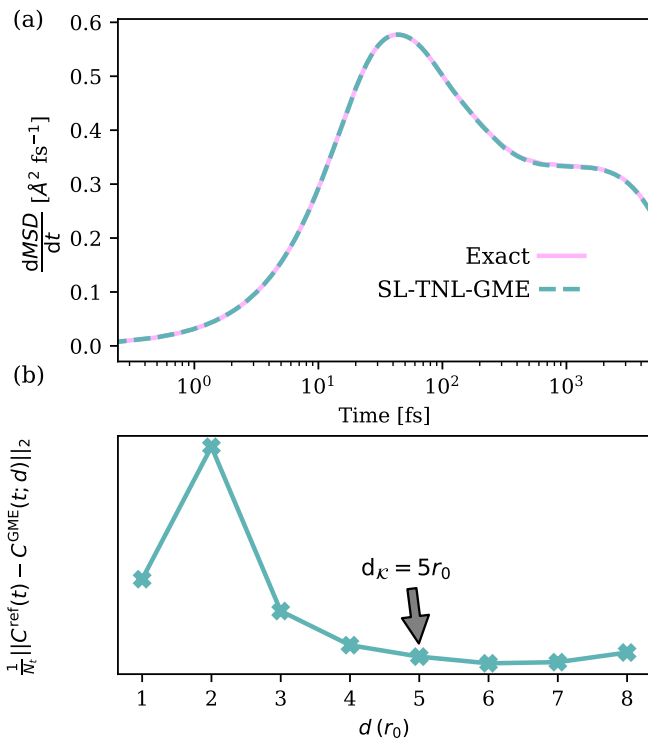


FIG. 14. Performance of the SL-TNL-GME for a dispersive Holstein lattice with  $N = 20$  sites and  $\eta = 323 \text{ cm}^{-1}$ ,  $v = 50 \text{ cm}^{-1}$  and  $\omega_c = 41 \text{ cm}^{-1}$ . (a) Our SL-TNL-GME (green dashed lines) recapitulates the reference simulation of  $d\text{MSD}/dt$  starting at  $d_\kappa = 5r_0$ . (b) Identification of the characteristic memory distance in the time-nonlocal framework from the deviation of the SL-TNL-GME from the reference dynamics as a function of the proposed distance cutoff.

## REFERENCES

- 1 T. Holstein, “Studies of polaron motion: Part i. the molecular-crystal model,” *Annals of Physics* **8**, 325–342 (1959).
- 2 T. Holstein, “Studies of polaron motion: Part II. The “small” polaron,” *Annals of Physics* **8**, 343–389 (1959).
- 3 H. Fröhlich, “Electrons in lattice fields,” *Advances in Physics* **3**, 325–361 (1954).
- 4 I. N. Hulea, S. Fratini, H. Xie, C. L. Mulder, N. N. Iossad, G. Rastelli, S. Ciuchi, and A. F. Morpurgo, “Tunable Fröhlich polarons in organic single-crystal transistors,” *Nature Materials* **5**, 982–986 (2006).
- 5 J. H. Fetherolf, D. Golež, and T. C. Berkelbach, “A Unification of the Holstein Polaron and Dynamic Disorder Pictures of Charge Transport in Organic Crystals,” *Physical Review X* **10**, 021062 (2020).
- 6 J. Hubbard, “Electron correlations in narrow energy bands,” *Proceedings of the Royal Society of London. Series A. Mathematical and Physical Sciences* **276**, 238–257 (1963).
- 7 E. Arrighoni, E. Fradkin, and S. A. Kivelson, “Mechanism of high-temperature superconductivity in a striped Hubbard model,” *Physical Review B* **69**, 214519 (2004).
- 8 E. Ising, “Beitrag zur theorie des ferromagnetismus,” *Zeitschrift für Physik* **31**, 253–258 (1925).
- 9 G. F. Newell and E. W. Montroll, “On the Theory of the Ising Model of Ferromagnetism,” *Reviews of Modern Physics* **25**, 353–389 (1953).
- 10 J. Dziarmaga, “Dynamics of a Quantum Phase Transition: Exact Solution of the Quantum Ising Model,” *Physical Review Letters* **95**, 245701 (2005).

- 11 Y. Tanimura and R. Kubo, “Time Evolution of a Quantum System in Contact with a Nearly Gaussian-Markoffian Noise Bath,” *Journal of the Physical Society of Japan* **58**, 101–114 (1989).
- 12 N. Makri and D. E. Makarov, “Tensor propagator for iterative quantum time evolution of reduced density matrices. II. Numerical methodology,” *The Journal of Chemical Physics* **102**, 4611–4618 (1995).
- 13 H. Wang, M. Thoss, and W. H. Miller, “Systematic convergence in the dynamical hybrid approach for complex systems: A numerically exact methodology,” *The Journal of Chemical Physics* **115**, 2979–2990 (2001).
- 14 M. Thoss, H. Wang, and W. H. Miller, “Self-consistent hybrid approach for complex systems: Application to the spin-boson model with Debye spectral density,” *The Journal of Chemical Physics* **115**, 2991–3005 (2001).
- 15 D. Suess, A. Eisfeld, and W. Strunz, “Hierarchy of Stochastic Pure States for Open Quantum System Dynamics,” *Physical Review Letters* **113**, 150403 (2014).
- 16 H. Wang, “Multilayer Multiconfiguration Time-Dependent Hartree Theory,” *The Journal of Physical Chemistry A* **119**, 7951–7965 (2015).
- 17 I. De Vega and M.-C. Bañuls, “Thermofield-based chain-mapping approach for open quantum systems,” *Physical Review A* **92**, 052116 (2015).
- 18 A. Strathearn, P. Kirton, D. Kilda, J. Keeling, and B. W. Lovett, “Efficient non-Markovian quantum dynamics using time-evolving matrix product operators,” *Nature Communications* **9**, 3322 (2018).
- 19 D. Tamascelli, A. Smirne, J. Lim, S. Huelga, and M. Plenio, “Efficient Simulation of Finite-Temperature Open Quantum Systems,” *Physical Review Letters* **123**, 090402 (2019).
- 20 F. A. Y. N. Schröder, D. H. P. Turban, A. J. Musser, N. D. M. Hine, and A. W. Chin, “Tensor network simulation of multi-environmental open quantum dynamics via machine learning and entanglement renormalisation,” *Nature Communications* **10**, 1062 (2019).
- 21 X. Xie, Y. Liu, Y. Yao, U. Schollwöck, C. Liu, and H. Ma, “Time-dependent density matrix renormalization group quantum dynamics for realistic chemical systems,” *The Journal of Chemical Physics* **151**, 224101 (2019).
- 22 B. Kloss, D. R. Reichman, and R. Tempelaar, “Multiset Matrix Product State Calculations Reveal Mobile Franck-Condon Excitations Under Strong Holstein-Type Coupling,” *Physical Review Letters* **123**, 126601 (2019).
- 23 N. Makri, “Small Matrix Path Integral with Extended Memory,” *Journal of Chemical Theory and Computation* **17**, 1–6 (2021).
- 24 A. Bose and P. L. Walters, “A multisite decomposition of the tensor network path integrals,” *The Journal of Chemical Physics* **156**, 024101 (2022).
- 25 D. Gribben, D. M. Rouse, J. Iles-Smith, A. Strathearn, H. Maguire, P. Kirton, A. Nazir, E. M. Gauger, and B. W. Lovett, “Exact Dynamics of Nonadditive Environments in Non-Markovian Open Quantum Systems,” *PRX Quantum* **3**, 010321 (2022).
- 26 G. E. Fux, D. Kilda, B. W. Lovett, and J. Keeling, “Tensor network simulation of chains of non-Markovian open quantum systems,” *Physical Review Research* **5**, 033078 (2023).
- 27 T. Lacroix, B. Le Dé, A. Riva, A. J. Dunnett, and A. W. Chin, “MPSDynamics.jl: Tensor network simulations for finite-temperature (non-Markovian) open quantum system dynamics,” *The Journal of Chemical Physics* **161**, 084116 (2024).
- 28 G. Kikugawa, T. Nakano, and T. Ohara, “Hydrodynamic consideration of the finite size effect on the self-diffusion coefficient in a periodic rectangular parallelepiped system,” *The Journal of Chemical Physics* **143**, 024507 (2015).
- 29 P. Simonnin, B. Noetinger, C. Nieto-Draghi, V. Marry, and B. Rotenberg, “Diffusion under Confinement: Hydrodynamic Finite-Size Effects in Simulation,” *Journal of Chemical Theory and Computation* **13**, 2881–2889 (2017).
- 30 S. J. Cox and P. L. Geissler, “Interfacial ion solvation: Obtain-

- ing the thermodynamic limit from molecular simulations,” *The Journal of Chemical Physics* **148**, 222823 (2018).
- <sup>31</sup>S. H. Jamali, L. Wolff, T. M. Becker, A. Bardow, T. J. H. Vlucht, and O. A. Moulτος, “Finite-Size Effects of Binary Mutual Diffusion Coefficients from Molecular Dynamics,” *Journal of Chemical Theory and Computation* **14**, 2667–2677 (2018).
  - <sup>32</sup>S. Samanta, S. Ghosh, and B. Mohanty, “Finite size effect of hadronic matter on its transport coefficients,” *Journal of Physics G: Nuclear and Particle Physics* **45**, 075101 (2018).
  - <sup>33</sup>B. Bertini, F. Heidrich-Meisner, C. Karrasch, T. Prosen, R. Steinigeweg, and M. Žnidarič, “Finite-temperature transport in one-dimensional quantum lattice models,” *Reviews of Modern Physics* **93**, 025003 (2021).
  - <sup>34</sup>A. T. Celebi, S. H. Jamali, A. Bardow, T. J. H. Vlucht, and O. A. Moulτος, “Finite-size effects of diffusion coefficients computed from molecular dynamics: a review of what we have learned so far,” *Molecular Simulation* **47**, 831–845 (2021).
  - <sup>35</sup>S. J. Cox and P. L. Geissler, “Dielectric response of thin water films: a thermodynamic perspective,” *Chemical Science* **13**, 9102–9111 (2022).
  - <sup>36</sup>P. Ray and K. Binder, “Finite-Size Effect in the Dynamics Near the Glass Transition,” *Europhysics Letters (EPL)* **27**, 53–58 (1994).
  - <sup>37</sup>L. Berthier, G. Biroli, D. Coslovich, W. Kob, and C. Toninelli, “Finite-size effects in the dynamics of glass-forming liquids,” *Physical Review E* **86**, 031502 (2012).
  - <sup>38</sup>G. Dos Santos, H. M. Urbassek, and E. M. Bringa, “Size-dependent Curie temperature of Ni nanoparticles from spin-lattice dynamics simulations,” *Scientific Reports* **14**, 22012 (2024).
  - <sup>39</sup>I.-C. Yeh and G. Hummer, “System-Size Dependence of Diffusion Coefficients and Viscosities from Molecular Dynamics Simulations with Periodic Boundary Conditions,” *The Journal of Physical Chemistry B* **108**, 15873–15879 (2004).
  - <sup>40</sup>F. Hébert, B. Xiao, V. G. Rousseau, R. T. Scalettar, and G. G. Batrouni, “One-dimensional Hubbard-Holstein model with finite-range electron-phonon coupling,” *Physical Review B* **99**, 075108 (2019).
  - <sup>41</sup>S. Bhattacharyya, T. Sayer, and A. Montoya-Castillo, “Anomalous Transport of Small Polarons Arises from Transient Lattice Relaxation or Immobile Boundaries,” *The Journal of Physical Chemistry Letters* **15**, 1382–1389 (2024).
  - <sup>42</sup>Q. Shi and E. Geva, “A new approach to calculating the memory kernel of the generalized quantum master equation for an arbitrary system–bath coupling,” *The Journal of Chemical Physics* **119**, 12063–12076 (2003).
  - <sup>43</sup>Q. Shi and E. Geva, “A semiclassical generalized quantum master equation for an arbitrary system–bath coupling,” *The Journal of Chemical Physics* **120**, 10647–10658 (2004).
  - <sup>44</sup>M.-L. Zhang, B. J. Ka, and E. Geva, “Nonequilibrium quantum dynamics in the condensed phase via the generalized quantum master equation,” *The Journal of Chemical Physics* **125**, 044106 (2006).
  - <sup>45</sup>G. Cohen and E. Rabani, “Memory effects in nonequilibrium quantum impurity models,” *Physical Review B* **84**, 075150 (2011).
  - <sup>46</sup>G. Cohen, E. Y. Wilner, and E. Rabani, “Generalized projected dynamics for non-system observables of non-equilibrium quantum impurity models,” *New Journal of Physics* **15**, 073018 (2013).
  - <sup>47</sup>A. Kelly and T. E. Markland, “Efficient and accurate surface hopping for long time nonadiabatic quantum dynamics,” *The Journal of Chemical Physics* **139**, 014104 (2013).
  - <sup>48</sup>L. Kidon, E. Y. Wilner, and E. Rabani, “Exact calculation of the time convolutionless master equation generator: Application to the nonequilibrium resonant level model,” *The Journal of Chemical Physics* **143**, 234110 (2015).
  - <sup>49</sup>A. Kelly, N. Brackbill, and T. E. Markland, “Accurate nonadiabatic quantum dynamics on the cheap: Making the most of mean field theory with master equations,” *The Journal of Chemical Physics* **142**, 094110 (2015).
  - <sup>50</sup>A. Kelly, A. Montoya-Castillo, L. Wang, and T. E. Markland, “Generalized quantum master equations in and out of equilibrium: When can one win?” *The Journal of Chemical Physics* **144**, 184105 (2016).
  - <sup>51</sup>A. Montoya-Castillo and D. R. Reichman, “Approximate but accurate quantum dynamics from the Mori formalism: I. Nonequilibrium dynamics,” *The Journal of Chemical Physics* **144**, 184104 (2016).
  - <sup>52</sup>W. C. Pfalzgraff, A. Montoya-Castillo, A. Kelly, and T. E. Markland, “Efficient construction of generalized master equation memory kernels for multi-state systems from nonadiabatic quantum-classical dynamics,” *The Journal of Chemical Physics* **150**, 244109 (2019).
  - <sup>53</sup>E. Mulvihill, X. Gao, Y. Liu, A. Schubert, B. D. Dunietz, and E. Geva, “Combining the mapping Hamiltonian linearized semiclassical approach with the generalized quantum master equation to simulate electronically nonadiabatic molecular dynamics,” *The Journal of Chemical Physics* **151**, 074103 (2019).
  - <sup>54</sup>N. Ng, D. T. Limmer, and E. Rabani, “Nonuniqueness of generalized quantum master equations for a single observable,” *The Journal of Chemical Physics* **155**, 156101 (2021).
  - <sup>55</sup>E. Mulvihill and E. Geva, “Simulating the dynamics of electronic observables via reduced-dimensionality generalized quantum master equations,” *The Journal of Chemical Physics* **156**, 044119 (2022).
  - <sup>56</sup>G. Amati, M. A. C. Saller, A. Kelly, and J. O. Richardson, “Quasiclassical approaches to the generalized quantum master equation,” *The Journal of Chemical Physics* **157**, 234103 (2022).
  - <sup>57</sup>N. Lyu, E. Mulvihill, M. B. Soley, E. Geva, and V. S. Batista, “Tensor-Train Thermo-Field Memory Kernels for Generalized Quantum Master Equations,” *Journal of Chemical Theory and Computation* **19**, 1111–1129 (2023).
  - <sup>58</sup>Y. Wang, E. Mulvihill, Z. Hu, N. Lyu, S. Shivpuje, Y. Liu, M. B. Soley, E. Geva, V. S. Batista, and S. Kais, “Simulating Open Quantum System Dynamics on NISQ Computers with Generalized Quantum Master Equations,” *Journal of Chemical Theory and Computation* **19**, 4851–4862 (2023).
  - <sup>59</sup>T. Sayer and A. Montoya-Castillo, “Compact and complete description of non-Markovian dynamics,” *The Journal of Chemical Physics* **158**, 014105 (2023).
  - <sup>60</sup>T. Sayer and A. Montoya-Castillo, “Efficient formulation of multitime generalized quantum master equations: Taming the cost of simulating 2D spectra,” *The Journal of Chemical Physics* **160**, 044108 (2024).
  - <sup>61</sup>T. Sayer and A. Montoya-Castillo, “Generalized quantum master equations can improve the accuracy of semiclassical predictions of multitime correlation functions,” *The Journal of Chemical Physics* **161**, 011101 (2024).
  - <sup>62</sup>S. Nakajima, “On Quantum Theory of Transport Phenomena: Steady Diffusion,” *Progress of Theoretical Physics* **20**, 948–959 (1958).
  - <sup>63</sup>R. Zwanzig, “Ensemble Method in the Theory of Irreversibility,” *The Journal of Chemical Physics* **33**, 1338–1341 (1960).
  - <sup>64</sup>H. Mori, “Transport, Collective Motion, and Brownian Motion,” *Progress of Theoretical Physics* **33**, 423–455 (1965).
  - <sup>65</sup>W. C. Pfalzgraff, A. Kelly, and T. E. Markland, “Nonadiabatic Dynamics in Atomistic Environments: Harnessing Quantum-Classical Theory with Generalized Quantum Master Equations,” *The Journal of Physical Chemistry Letters* **6**, 4743–4748 (2015).
  - <sup>66</sup>Y. Liu, E. Mulvihill, and E. Geva, “Combining the generalized quantum master equation approach with quasiclassical mapping Hamiltonian methods to simulate the dynamics of electronic coherences,” *The Journal of Chemical Physics* **161**, 164101 (2024).
  - <sup>67</sup>S. Cao, A. Montoya-Castillo, W. Wang, T. E. Markland, and X. Huang, “On the advantages of exploiting memory in Markov state models for biomolecular dynamics,” *The Journal of Chemical Physics* **153**, 014105 (2020).
  - <sup>68</sup>A. J. Dominic, T. Sayer, S. Cao, T. E. Markland, X. Huang,

- and A. Montoya-Castillo, "Building insightful, memory-enriched models to capture long-time biochemical processes from short-time simulations," *Proceedings of the National Academy of Sciences* **120**, e2221048120 (2023).
- <sup>69</sup>S. Cao, Y. Qiu, M. L. Kalin, and X. Huang, "Integrative generalized master equation: A method to study long-timescale biomolecular dynamics via the integrals of memory kernels," *The Journal of Chemical Physics* **159**, 134106 (2023).
- <sup>70</sup>A. Ivanov and H.-P. Breuer, "Extension of the Nakajima-Zwanzig approach to multitime correlation functions of open systems," *Physical Review A* **92**, 032113 (2015).
- <sup>71</sup>Y. Yan, M. Xu, Y. Liu, and Q. Shi, "Theoretical study of charge carrier transport in organic molecular crystals using the Nakajima-Zwanzig-Mori generalized master equation," *The Journal of Chemical Physics* **150**, 234101 (2019).
- <sup>72</sup>S. Bhattacharyya, T. Sayer, and A. Montoya-Castillo, "Mori generalized master equations offer an efficient route to predict and interpret polaron transport," *Chemical Science* **15**, 16715–16723 (2024).
- <sup>73</sup>Y.-C. Cheng and R. J. Silbey, "A unified theory for charge-carrier transport in organic crystals," *The Journal of Chemical Physics* **128**, 114713 (2008).
- <sup>74</sup>M. B. Qarai, R. Ghosh, and F. C. Spano, "Understanding Bipolarons in Conjugated Polymers Using a Multiparticle Holstein Approach," *The Journal of Physical Chemistry C* **125**, 24487–24497 (2021).
- <sup>75</sup>H. Mousavi and M. Bagheri, "Effects of Holstein phonons on the electrical conductivity of carbon nanotubes," *Physica E: Low-dimensional Systems and Nanostructures* **44**, 1722–1724 (2012).
- <sup>76</sup>G. D. Mahan, *Many-Particle Physics* (Springer US, Boston, MA, 2000).
- <sup>77</sup>M. Z. Mayers, L. Z. Tan, D. A. Egger, A. M. Rappe, and D. R. Reichman, "How Lattice and Charge Fluctuations Control Carrier Dynamics in Halide Perovskites," *Nano Letters* **18**, 8041–8046 (2018).
- <sup>78</sup>T. Nematiram and A. Troisi, "Modeling charge transport in high-mobility molecular semiconductors: Balancing electronic structure and quantum dynamics methods with the help of experiments," *The Journal of Chemical Physics* **152**, 190902 (2020).
- <sup>79</sup>S. Krylow, F. V. Hernandez, B. Bauerhenne, and M. E. Garcia, "Ultrafast structural relaxation dynamics of laser-excited graphene: *Ab initio* molecular dynamics simulations including electron-phonon interactions," *Physical Review B* **101**, 205428 (2020).
- <sup>80</sup>H. Li, M. Guo, Z. Zhou, R. Long, and W.-H. Fang, "Excitation-Wavelength-Dependent Charge-Carrier Lifetime in Hematite: An Insight from Nonadiabatic Molecular Dynamics," *The Journal of Physical Chemistry Letters* **14**, 2448–2454 (2023).
- <sup>81</sup>U. Weiss, *Quantum dissipative systems* (World Scientific, 2012).
- <sup>82</sup>Q. Shi, L. Chen, G. Nan, R.-X. Xu, and Y. Yan, "Efficient hierarchical Liouville space propagator to quantum dissipative dynamics," *The Journal of Chemical Physics* **130**, 084105 (2009).
- <sup>83</sup>H. Liu, L. Zhu, S. Bai, and Q. Shi, "Reduced quantum dynamics with arbitrary bath spectral densities: Hierarchical equations of motion based on several different bath decomposition schemes," *The Journal of Chemical Physics* **140**, 134106 (2014).
- <sup>84</sup>K. Song, S. Bai, and Q. Shi, "A time domain two-particle approximation to calculate the absorption and circular dichroism line shapes of molecular aggregates," *The Journal of Chemical Physics* **143**, 064109 (2015).
- <sup>85</sup>L. Song and Q. Shi, "A new approach to calculate charge carrier transport mobility in organic molecular crystals from imaginary time path integral simulations," *The Journal of Chemical Physics* **142**, 174103 (2015).
- <sup>86</sup>P. Debye and E. Hückel, "De la theorie des electrolytes. i. abaissement du point de congelation et phenomenes associes," *Physikalische Zeitschrift* **24**, 185–206 (1923).
- <sup>87</sup>J. G. Kirkwood, "Statistical Mechanics of Liquid Solutions," *Chemical Reviews* **19**, 275–307 (1936).
- <sup>88</sup>J. Rowlinson, "The Yukawa potential," *Physica A: Statistical Mechanics and its Applications* **156**, 15–34 (1989).
- <sup>89</sup>N. B. Ludwig, K. Dasbiswas, D. V. Talapin, and S. Vaikuntanathan, "Describing screening in dense ionic fluids with a charge-frustrated Ising model," *The Journal of Chemical Physics* **149**, 164505 (2018).
- <sup>90</sup>B. Rotenberg, O. Bernard, and J.-P. Hansen, "Underscreening in ionic liquids: a first principles analysis," *Journal of Physics: Condensed Matter* **30**, 054005 (2018).
- <sup>91</sup>A. Härtel, M. Bültmann, and F. Coupette, "Anomalous Underscreening in the Restricted Primitive Model," *Physical Review Letters* **130**, 108202 (2023).
- <sup>92</sup>J. Yang, S. Kondrat, C. Lian, H. Liu, A. Schlaich, and C. Holm, "Solvent effects on structure and screening in confined electrolytes," *Physical Review Letters* **131**, 118201 (2023).
- <sup>93</sup>M. Dinpajoo, E. Biasin, E. T. Nienhuis, S. T. Mergelsberg, C. J. Benmore, G. K. Schenter, J. L. Fulton, S. M. Kathmann, and C. J. Mundy, "Detecting underscreening and generalized Kirkwood transitions in aqueous electrolytes," *The Journal of Chemical Physics* **161**, 151102 (2024).
- <sup>94</sup>The sublinear scaling in time arises from the ability to exploit the group property of the generator to obtain an effective generator over a larger timestep beyond the onset of Markovian behavior:  $\mathcal{U}(n\delta t) = [\mathcal{U}(\delta t)]^n$ .
- <sup>95</sup>A. Chernikov, T. C. Berkelbach, H. M. Hill, A. Rigosi, Y. Li, B. Aslan, D. R. Reichman, M. S. Hybertsen, and T. F. Heinz, "Exciton Binding Energy and Nonhydrogenic Rydberg Series in Monolayer WS<sub>2</sub>," *Physical Review Letters* **113**, 076802 (2014).
- <sup>96</sup>Y. Wan, Z. Guo, T. Zhu, S. Yan, J. Johnson, and L. Huang, "Cooperative singlet and triplet exciton transport in tetracene crystals visualized by ultrafast microscopy," *Nature Chemistry* **7**, 785–792 (2015).
- <sup>97</sup>S. J. Yoon, Z. Guo, P. C. Dos Santos Claro, E. V. Shevchenko, and L. Huang, "Direct Imaging of Long-Range Exciton Transport in Quantum Dot Superlattices by Ultrafast Microscopy," *ACS Nano* **10**, 7208–7215 (2016).
- <sup>98</sup>Z. Guo, Y. Wan, M. Yang, J. Snider, K. Zhu, and L. Huang, "Long-range hot-carrier transport in hybrid perovskites visualized by ultrafast microscopy," *Science* **356**, 59–62 (2017).
- <sup>99</sup>C. L. Kennedy, A. H. Hill, E. S. Massaro, and E. M. Grumstrup, "Ultrafast Excited-State Transport and Decay Dynamics in Cesium Lead Mixed Halide Perovskites," *ACS Energy Letters* **2**, 1501–1506 (2017).
- <sup>100</sup>A. H. Hill, K. E. Smyser, C. L. Kennedy, E. S. Massaro, and E. M. Grumstrup, "Screened Charge Carrier Transport in Methylammonium Lead Iodide Perovskite Thin Films," *The Journal of Physical Chemistry Letters* **8**, 948–953 (2017).
- <sup>101</sup>M. Delor, H. L. Weaver, Q. Yu, and N. S. Ginsberg, "Imaging material functionality through three-dimensional nanoscale tracking of energy flow," *Nature Materials* **19**, 56–62 (2020).
- <sup>102</sup>N. S. Ginsberg and W. A. Tisdale, "Spatially Resolved Photogenerated Exciton and Charge Transport in Emerging Semiconductors," *Annual Review of Physical Chemistry* **71**, 1–30 (2020).
- <sup>103</sup>P. R. Bueno and J. J. Davis, "Charge transport and energy storage at the molecular scale: from nanoelectronics to electrochemical sensing," *Chemical Society Reviews* **49**, 7505–7515 (2020).
- <sup>104</sup>H. Zhang, Y. Geng, J. Huang, Z. Wang, K. Du, and H. Li, "Charge and mass transport mechanisms in two-dimensional covalent organic frameworks (2D COFs) for electrochemical energy storage devices," *Energy & Environmental Science* **16**, 889–951 (2023).
- <sup>105</sup>H. Liu, A. Wang, P. Zhang, C. Ma, C. Chen, Z. Liu, Y.-Q. Zhang, B. Feng, P. Cheng, J. Zhao, L. Chen, and K. Wu, "Atomic-scale manipulation of single-polaron in a two-dimensional semiconductor," *Nature Communications* **14**, 3690 (2023).
- <sup>106</sup>C. E. Schwarz, R. S. Saravanan, N. M. Borodin, Y. Liu, E. D. Wachsman, and Y. Mo, "Polaron-Based Electronic Conduction

- in Mixed Ionic-Electronic Conducting Lithium Garnets,” *ACS Energy Letters* **9**, 5334–5340 (2024).
- <sup>107</sup>A. Troisi, “Prediction of the Absolute Charge Mobility of Molecular Semiconductors: the Case of Rubrene,” *Advanced Materials* **19**, 2000–2004 (2007).
- <sup>108</sup>J. Cerrillo and J. Cao, “Non-Markovian Dynamical Maps: Numerical Processing of Open Quantum Trajectories,” *Physical Review Letters* **112**, 110401 (2014).
- <sup>109</sup>G. Stock and M. Thoss, “Semiclassical Description of Nonadiabatic Quantum Dynamics,” *Physical Review Letters* **78**, 578–581 (1997).
- <sup>110</sup>X. Sun, H. Wang, and W. H. Miller, “Semiclassical theory of electronically nonadiabatic dynamics: Results of a linearized approximation to the initial value representation,” *The Journal of Chemical Physics* **109**, 7064–7074 (1998).
- <sup>111</sup>W. H. Miller, “Electronically Nonadiabatic Dynamics via Semiclassical Initial Value Methods,” *The Journal of Physical Chemistry A* **113**, 1405–1415 (2009).
- <sup>112</sup>S. Bhattacharyya, T. Sayer, and A. Montoya-Castillo, “Nonequilibrium relaxation exponentially delays the onset of quantum diffusion,” (in preparation).
- <sup>113</sup>H. Grabert, *Projection Operator Techniques in Nonequilibrium Statistical Mechanics*, Springer Tracts in Modern Physics, Vol. 95 (Springer Berlin Heidelberg, Berlin, Heidelberg, 1982).
- <sup>114</sup>M. Sparpaglione and S. Mukamel, “Dielectric friction and the transition from adiabatic to nonadiabatic electron transfer. I. Solvation dynamics in Liouville space,” *The Journal of Chemical Physics* **88**, 3263–3280 (1988).
- <sup>115</sup>S. M. Greene and V. S. Batista, “Tensor-Train Split-Operator Fourier Transform (TT-SOFT) Method: Multidimensional Nonadiabatic Quantum Dynamics,” *Journal of Chemical Theory and Computation* **13**, 4034–4042 (2017).